Title

Node-Pore Coded Coincidence Correction: Coulter Counters, Code Design, and Sparse Deconvolution

Journal

IEEE Sensors Journal, 18(8)

ISSN

1530-437X

Authors

Kellman, Michael R
Rivest, Francois R
Pechacek, Alina
et al.

Publication Date

2018-04-15

DOI

10.1109/jsen.2018.2805865

Peer reviewed

HHS Public Access
Author manuscript
IEEE Sens J. Author manuscript; available in PMC 2019 April 15.

Published in final edited form as:
IEEE Sens J. 2018 April 15; 18(8): 3068–3079. doi:10.1109/JSEN.2018.2805865.

Node-Pore Coded Coincidence Correction: Coulter Counters, Code Design, and Sparse Deconvolution

Michael Kellman[*], **Francois Rivest**[†,§], **Alina Pechacek**[*], **Lydia Sohn**[†,‡], and **Michael Lustig**[*,‡]

[*]Dept. of Electrical Engineering and Computer Sciences, University of California, Berkeley [†]Dept. of Mechanical Engineering, University of California, Berkeley [§]Institute of Bioengineering, Ecole Polytechnique Federale de Lausanne, Switzerland [‡]Graduate Program in Bioengineering, University of California Berkeley, Berkeley, CA, USA

Abstract

We present a novel method to perform individual particle (e.g. cells or viruses) coincidence correction through joint channel design and algorithmic methods. Inspired by multiple-user communication theory, we modulate the channel response, with Node-Pore Sensing, to give each particle a binary Barker code signature. When processed with our modified successive interference cancellation method, this signature enables both the separation of coincidence particles and a high sensitivity to small particles. We identify several sources of modeling error and mitigate most effects using a data-driven self-calibration step and robust regression. Additionally, we provide simulation analysis to highlight our robustness, as well as our limitations, to these sources of stochastic system model error. Finally, we conduct experimental validation of our techniques using several encoded devices to screen a heterogeneous sample of several size particles.

Keywords

Coincidence Correction; Barker Codes; Node-Pore Sensing; Inverse Problems; Successive Interference Cancellation; Coulter Counter; Computational Sensing

I. Introduction

The Coulter principle [1] is a ubiquitous method for accurately measuring the number and size of particles in a solution [2]. The method is based on detecting and measuring a current pulse generated by a particle (e.g. cells or viruses), suspended in an electrolyte solution, as it flows through an aperture or channel that has an applied voltage potential across it. Since its inception in the 1950's, the Coulter principle has been used in a number of diverse applications, from biomedical (e.g. automated red blood cell counting [3], [4], [5], viral/pathogen detection [6], [7], [8], [9], [10], [11], DNA detection [12], [13], [14], [15], [16], [17]) to industrial applications (e.g. food [18], cosmetics [19]). Key to many of these applications is that the size of the aperture or channel width must be commensurate to that of the particles to be measured in order to ensure a high signal-to-noise ratio (SNR). In the case

Corresponding Author: Prof. Michael Lustig (mlustig@berkeley.edu).

of measuring a heterogeneous mixture, when too small of an aperture or channel width is used, larger-sized particles can lead to clogging. Conversely, when too large an aperture or channel width is used, smaller-sized particles may go undetected due to low SNR. Thus, despite the overall simplicity and wide utility of the Coulter principle, challenges still exist.

Another well-recognized design challenge for any appropriately sized aperture or channel width is that arising from coincidence events[3], [20], [21], [22], i.e. when two or more particles enter the sensing region simultaneously. Such events lead to errors whose level of severity depends on the degree at which coincidence occur: almost no overlap, horizontal coincidence (Fig. 1b), to partial overlap (Fig. 1c), to extreme overlap, vertical coincidence (Fig. 1d). In general, coincidence events lead to ambiguities in detection, error in size (and, in turn, incorrect size distributions in a population), and missed rare events. Coincidence corrections range from simple removal of the particular detection to complex algorithms [20], [21], [23], [24], [25].

Correction of these errors can be compensated statistically by estimating the expected number of detection counts that were coincident events. This is achieved by modeling the expected number of particles in the sensing region as a Poisson process, parametric with the volume of the sensing region and number of detections [20], [21], [23]. Another correction involves screening the same sample at several known dilutions and then computing the actual count as well as the rate of coincidence events [24], [25]. Today, commercial Coulter counters utilize the first method to statistically perform coincidence correction [26], [27], [28], based on the number of particles detected and volume of the sensing region. While these methods might be accurate for correcting distributions, they do not resolve individual coincidence events. This is problematic when detecting specific and small sub-populations or rare cell events [6].

With the goal of achieving individual particle coincidence correction for applications of high-throughput screening, several impedance-based multi-channel designs have been proposed, each of which relies upon a unique signal-encoding mechanism (e.g. individual sensing electrodes [29], frequency-division multiplexing [30], orthogonal-code-division multiplexing with co-planar electrodes [31], [32]) that ultimately gives each channel of the device a signature enabling separation. While these designs allow the detection and separation of particles simultaneously transiting different channels, they fail to provide adequate coincidence correction when two or more particles transit the same channel simultaneously. Then to achieve the goal of a higher sensitivity to smaller particles, that would otherwise have SNR too low to detect, several single-channel designs have been proposed, each relying upon, again, a signal-encoding mechanism (e.g. channel sidewall modulation [33], electrodes on top and bottom of the channel [34], co-planar electrodes [35]). However, these methods do not enable individual particle coincidence correction.

Recently, a work by Liu et al.[31], [32] developed an approach that can perform the separation of coincidence particles transiting spatially-multiplexed channels based on the principles of code-division-multiple-access (CDMA) from communication theory. Their solution is part enabled by their electrode-encoding mechanism that differentially encodes each channel with a quasi-orthogonal signature and in part by their iterative interference cancellation algorithm. Their method is successful in separating coincidence corrections, but requires complex circuit-system modeling to properly calibrate the system [32] and their choice of binary codes have sub-optimal separation properties for coincidence correction within a single channel. This work extends earlier work by Kellman et al. [36].

We propose a joint channel design and processing framework that achieves high sensitivity for small particles and individual particle coincidence correction, while maintaining only a single external measurement and a single channel configuration. By modeling the single microfluidic channel as a communication system that encodes passing particle signals like packets of information, we can apply the signal processing from multi-user communication theory [37] to detect and separate particles in coincidence settings. Specifically, we achieve this by amplitude modulating our channel response with Node-Pore Sensing [38], [39] (NPS) to generate a modified Barker [40] binary-code sequence. The Barker code's structure allows us to take advantage of its optimal quasi-orthogonal properties to resolve coincidences. Furthermore, with its special filtering properties, we can also achieve a gain in SNR, thereby providing a higher sensitivity to smaller particles.

We formulate the coincidence correction problem as a sparse deconvolution inverse problem and exploit the channel design and sparsity of particles flowing through the channel to provide an efficient solution via a successive interference cancellation (SIC) algorithm. With analysis, we highlight the robustness, as well as the limitations, of our method to several sources of stochastic system model error and experimental error. Additionally, we propose modifications to the SIC algorithm, which include a data-driven system model calibration step and a robust particle size estimate step, to mitigate the effects of system model error. Experimental validation is performed via the fabrication and measurement of several encoded devices and subsequent screening of heterogeneous samples. Finally, we discuss how to pick which length code to use, other coding schemes, and other sources of system modeling error.

II. Coding Microfluidic Channels

Balakrishnan et al. [38], [39] previously demonstrated that impedance measurements of a microfluidic channel can be modulated by fabricating channels with locally wider (nodes) and narrower (pores) regions in specific sequences (Fig. 2a), hereafter referred to as NPS channels. As a particle transits from a node to a pore, the impedance response will increase proportionally to the ratio between the particle's volume and the pore's cross sectional area [41] as described in Equation 1 where R is the baseline impedance, ΔR is the increase in impedance, d is the diameter of the particle, L is the length of the channel, and D is the effective diameter of the channel.

$$\frac{\Delta R}{R} = \frac{d^3}{LD^2}\frac{1}{1 - 0.8\left(\frac{d}{D}\right)^3} \quad (1)$$

Because a node's cross sectional area is much larger than the particle, as a particle transits from a pore to a node, the impedance response will nearly return to baseline (Fig. 2b), thus enabling the impedance response's binary amplitude modulation. Similar to the binary amplitude modulation used in communication systems [42], NPS coding can be used as the general encoding mechanism to provide structure in the system response of microfluidic channels[39].

We utilize the flexibility of NPS channel encoding to amplitude modulate our channel's response with the Barker coding scheme: a binary sequence ubiquitous in communication systems (e.g. Direct Sequence Spread Spectrum in 802.11b Wi-Fi [42] and in radar for high-resolution detection and ranging [43]). To describe the encoding scheme's unique properties, it is useful to draw on analogies between Barker-coded NPS channels and classic communication theory. Thus, in the terminology of communication theory, the measured signal response of a single node or pore, with its associated transit time (τ), is a symbol and the bandwidth (BW) of the channel's encoding or symbol-rate is one over the symbol's transit time (i.e. $BW = \frac{1}{\tau}$).

The central appealing property of the Barker-coding scheme is its quasi-orthogonality (referred to as pulse compression in communication theory), such that when correlated with its model, the response gives a focused high-energy peak at the point of perfect overlap and a minimal response at all other shifts (side-lobes) (Fig. 2c). The full width half max (FWHM) of the peak, referred to as the temporal resolution, is proportional to the transit time of a single symbol and represents the minimum distance by which two particles can be separated. Additionally, the height of the peak represents the gain in SNR we expect and is proportional to the square root of the number of symbols divided by the bandwidth (i.e. $\text{gain} = \sqrt{\frac{\#symbol}{BW}}$). The bandwidth of our encoding scheme can be controlled via the speed of particles flowing through the channel and by the dimensions of the channel.

Due to the one-sided nature of our amplitude modulated impedance signal, we took a similar approach to Levanon et al. [44] and adapted the Barker code by encoding its bit-values in signal transitions, Manchester encoding [45] (i.e. +1 as high-to-low transition, -1 as low-to-high transition). Impedance transitions from high-to-low are achieved with a pore-node sequence and low-to-high with a node-pore sequence. The combined Manchester-Barker code, hereafter referred to as MB codes, is shown in Figure 2b. The result is a binary sequence that is double in length and has similar properties in terms of the quasi-orthogonality and SNR gain to that of the traditional Barker code when correlated with the model, hereafter referred to as matched filtering (highlighted in Figure 2c).

III. Algorithmic Methods

A. System Modeling

As a particle transits the channel at constant pressure, it generates an impedance signal response that depends on the node-pore encoding, the length of the channel, and the velocity of the particle. If a similar particle transits the channel at another time with the same velocity, it will produce a similar impedance signal response. If a particle has a different velocity, from following a different velocity streamline or due to interactions with the channel sides, the impedance response will have a similar shape, but will be dilated or compressed in time. Furthermore, if in a coincidence event, the impedance signal response will be the superposition of their respective impedances had each particle transited the channel individually. Thus, the impedance measurement of the channel response (y_t) for particles passing through the channel can be well approximated as a linear time-invariant (LTI) system that is parametrized by each particle's transit time. This allows particles transiting the channel to be modeled as a convolution of a time-dilated system response (h_τ) with a series of scaled impulse functions (x_t) (Fig. 3a-b). Each impulse represents the arrival time and the signal amplitude that is proportional to the associated particle's size. In addition, a time-varying affine term is added to account for slow time-varying baseline drift (b_t). Finally, we include an additive Gaussian noise term (n_t), which we assume to have zero mean and variance corresponding to sensor noise.

$$y_t = h_\tau * x_t + b_t + n_t \qquad (2)$$

A discretization of the problem can be formulated in matrix form as

$$y = Ax + b + n, \qquad (3)$$

where the columns of A consist of unit-amplitude shifted and dilated dictionary of channel responses for a range of transit-times and x a sparse vector in which each non-zero element represents the signal amplitude of an individual particle and which indices represent an individual particle's arrival-time and transit-time. This system model is illustrated in Figure 3c.

B. Inverse Problem Formulation

The problem of estimating particles' signal amplitudes, arrival times, and transit times can be viewed as a deconvolution. While unconstrained deconvolution is in general a difficult problem, in this case, the number of particles passing through the channel is statistically bounded by the channel length and the particle concentration within the solution. Therefore, we can pose the deconvolution as the following cardinality constrained linear inverse problem,

$$\begin{aligned} \min_{x,b} \quad & \|Ax + b - y\|_2 + \lambda \|Db\|_2 \\ \text{s.t.} \quad & \text{cardinality}\{x \in range(t, \tau)\} < k \end{aligned} \qquad (6)$$

in which the number of particles transiting the channel, cardinality$\{x \in range(t, \tau)\}$, in a fixed period of time is constrained by k. We solve Equation 4 for approximately sparse entries in x which correspond to arrival and transit time with amplitude proportional to the size of the particle. We also simultaneously solve for the baseline term, b, which is constrained to be smooth using the ℓ_2 regularization of its second-order difference. This difference operator is represented by D. The parameter λ controls the bandwidth of the estimated baseline and is empirically tuned to penalize the high-frequency spectrum of the baseline signal to not allow cross-talk between the values of x_i and b.

C. Implementation of Successive Interference Cancellation

To reduce the computational complexity of the process, we break the input signal into overlapping blocks. Each block is processed separately, and the results are consolidated at the end. For each block, we solve the sparse deconvolution using a greedy successive interference cancellation algorithm, similar to orthogonal matching pursuit [46]. Figure 4a illustrates our method. It is outlined by iterating a sequence of correlations with a matched filter-bank (*i.e.*, the dictionary), detection, model fitting, and cancellation steps. Over the iterations we construct a list of the strongest detections, referred to as the list of detected signal components. We grow the list by adding the strongest unique detection every iteration. Each iteration we jointly fit all detected signal model components and a smooth baseline term to the data to estimate the particles' impedance signal amplitudes. By cancelling/peeling the strongest signal in each iteration, we allow for the impedance response of smaller particles to be detected in successive rounds. Figure 4b is one example of experimental data (outlined in Section V) of a coincidence of three particles (one of size 15μm and two of size 10μm) transiting through a MB length 13 encoded channel and Figure 4c illustrates three iterations of the SIC algorithm.

D. Basic Methodology

In this section, we first describe a basic approach for implementing the SIC algorithm. Figure 4c demonstrates several iterations of the algorithm on a block of experimental data. First, we apply the transpose, *i.e.* A^T, matrix to the data, hereafter referred to as the matched filter-bank response, or correlation map $c(t, \tau)$ parametrized by arrival times t and transit times τ. This operation is equivalent to filtering with a matched filter-bank of time-dilated and time-contracted MB codes. The filter bank is comprised of normalized filters each with a unique transit time parameter such that the continuous parameter space is linearly discretized over a range of plausible particle transit times. The number of filters in the filter bank determines the resolution of transit-time parameter estimate and thus effects the computation complexity as well as accuracy of our method, this is discussed further in Section VI-C. The top row of Figure 4c shows the filter-bank response, in which the dominating peak indicates a particle's presence, and red circle indicates its detection. The small black arrowheads indicate peaks that are initially obscured by the signal interference from the large particle, to be later revealed through the peeling process.

We adopt an adaptive threshold detection scheme [43] that is performed on the matched filter-bank response to localize a particle's arrival and transit time parameters. The large dynamic range of particle sizes could yield different levels of ‘true-peaks’ corresponding to actual particles, and ‘false-peaks’ corresponding to sidelobes of the matched filter-bank response. Therefore an adaptive scheme is necessary to manage false alarms and mis-detections in a signal with a wide dynamic range of particle sizes. Our adaptive detection scheme is motivated by the constant false alarm rate criteria [47], where each correlation value $c(t, \tau)$ is evaluated against a threshold derived from an estimate of the surrounding signal energy. Let $\varepsilon(t_0, \tau_0)$ be a function that computes a surrounding signal energy of the correlation function $c(t, \tau)$ in a window around $t = t_0$ and $\tau = \tau_0$. In this case, the criteria for detection at point (t_0, τ_0) is set to be

$$c\left(t_0, \tau_0\right) > \alpha\varepsilon\left(t_0, \tau_0\right), \quad (5)$$

where α is a tuning parameter. Robust estimates of the surrounding signal energy function as well as selections of α are further discussed in Supplementary.

The detection scheme chooses a list of possible candidate detections, from which a single unique detection, corresponding to the greatest correlation value, is selected for each iteration. The transit-time and arrival-time estimates for a detection are chosen to correspond to that of the best correlating filter in the matched filter bank and the time point when that matched filter response is maximum. Once a detection is added to the list, the amplitude of all the detected particles are re-evaluated using a least-square regression. The middle row of Figure 4c shows examples of resulting fits. More formally, we define $\tilde{A}_i$, to be a subset of columns of A corresponding to signal responses of detected particles by the i^{th} iteration, and $\tilde{x}_i \in \mathbb{R}^i$ to be the unknown signal amplitudes of the subset of detected peaks by the i^{th} iteration. In this case, the entire least-squares fit at the i^{th} iteration is formulated as,

$$\min_{\tilde{x}_i, b} \left\|\tilde{A}_i \tilde{x}_i + b - y\right\|_2 + \lambda \left\|Db\right\|_2 \quad (6)$$

In each iteration we only solve for a few variables and the baseline and hence the computation complexity of this portion of the algorithm is low.

Finally, the time signals of the detected particles are computed and subtracted from the acquired signal by computing $r = y - \tilde{A}_i\tilde{x}_i$. This is illustrated in the bottom row of Figure 4c. This residual is used as an input to the next iteration for the purpose of possibly detecting other particles of equal or lesser size.

This process is repeated until either of the stopping conditions, *i.e.*, no more significant detections in the block or the process reaches the k^{th} iteration of SIC are met. The second stopping criteria enforces the cardinality constraint from Equation 4. Finally, in post-processing, the particle sizes are computed as a function of channel dimensions and pulse height [41] via Equation 1.

IV. Sources of Model Error

The bottom row of Figure 4c illustrates that the interference cancelled signals at each iteration have sparse outlier residuals. The presence of sparse residual outliers could possibly introduce biases into the least-square particle size estimates, errors in the arrival-time and transit-time estimates, and detections errors. These sparse outlier residuals cannot be fit by varying the amplitude or transit time of the signal components and thus are a result of modeling error (discrepancies between the ideal and measured MB signals). The discrepancies can be separated into two components; average and stochastic. The average deviation affects all particles equally and could result from channel geometry variation or be due to miscalculations between the ideal code and the actual device. The stochastic deviations are small deviations from the model and could arise from random interactions between the particle and the channel. This could be caused by particles travelling along streamlines with different flow-rates; such streamlines could be the result of parabolic flow effects[48].

A. System Model Calibration

To model the average deviation effect, we use a data-driven calibration step in which we empirically recalculate the symbol lengths of our MB code to match the average impedance response of particles that go through the channel. The calibration is achieved by performing a first pass of detecting high SNR particles (15μm particles in our experiments outlined in Section V) using the ideal matched filter bank. For each of the detected signatures, we look at the transit time of each node and pore of the MB code, specifically the number of samples between signal transitions normalized by the total number of samples of the MB code signature. This scale invariant measure is then used to compare between the detected particle signatures and to generate a calibrated model through regression. In our list of detections, a small number of the high SNR signals are also coincidence events, thus introducing possibly incorrect symbol timing measurements into the calibration. To enable our calibration to be robust to these outlier events, we perform a robust regression [49] rather than a least-squares regression, by utilizing an ℓ_1-norm rather than an ℓ_2-norm as seen in equation 7.

$$\arg\min_{z_{\text{cal}}} \sum_{i=0}^{N-1} \left\| z_i - z_{\text{cal}} \right\|_1 . \quad (7)$$

Where z_i is the vector of normalized symbol timings for the i^{th} detection and we solve for the calibrated MB code timings, z_{cal}. Once the calibrated MB code model is estimated, a new matched filter bank is generated.

B. Robust Regression Formulation of SIC

Even with the steps described above, we will still have stochastic variation in the transit of particles that would result in model mismatches between our data and calibrated MB codes. These mismatches will manifest as outlier residuals, which can be seen clearly in Fig. 4c. These sparse outliers can introduce bias into the estimation of the pulse amplitudes. To reduce this bias, we turn again to a robust regression [49] approach with the following formulation,

$$\min_{\tilde{x}_i, b} \left\| \tilde{A}_i \tilde{x}_i + b - y \right\|_1 + \lambda \left\| Db \right\|_2 . \quad (8)$$

In our implementation we solve the robust regression via an iterative re-weighted least-squares (IRLS) [50] approach (See Supplementary).

V. Experimental Methods

A. Device Fabrication

Similar to those outlined in Balakrishnan's et al.[39], we employed standard micro-fabrication techniques to fabricate planar electrodes onto glass substrates. These electrodes allow us to perform a four-probe measurement to sense the current through the entire MB-coded NPS device. Further, we employed standard soft-lithographic techniques to embed our MB-coded channel in polydimethylsiloxane (PDMS) slabs (See Supplementary). We implemented three different MB-length codes: 7, 11, and 13. We chose the channel height to be 20μm and overall length as 4 mm. We varied the width of the pores and nodes to maintain a 2.5 ratio of node-to-pore width to ensure the signal would return to baseline when particles transit from pore to node. Specifically, pores are designed to be 20μm wide and nodes are designed to be 50μm wide. We also kept a 2.5 pore-to-node length ratio to maintain an equal transit time of particles in nodes and pores (illustrated in Figure 6). This ensures that the recorded pulses have an equal number of samples in the impedance response for each symbol of a particle's signature (illustrated in Figure 2b). A discussion of channel dimension limits is continued in Section VII. To seal the devices, we exposed both the PDMS slabs and glass substrates with the pre-fabricated electrodes (See Supplementary) to oxygen plasma (300mT, 80W, 30sec), aligned the two together, and then permanently bond the PDMS and glass substrate by heating at 80° C for 30 minutes.

B. Experimental Setup

We applied a 1V DC voltage across the device and passed the measured current signal through a current preamplifier (DL Instruments 1211, Brooktondale, NY, USA) to a data acquisition (DAQ) board (National Instrument PCI-6035E, Austin, TX, USA). The DAQ sampled the analog signal at a rate of 50 kHz.

We screened a 1 : 1 : 1 ratio mixture of polystyrene microspheres with mean and standard deviation diameter: $\mu = 4.9\mu m$, $\sigma = 0.44\mu m$ (Interfacial Dynamics 1-5000), $\mu = 9.98\mu m$, $\sigma = 1.12\mu m$ (Polysciences Inc. 64130), and $\mu = 14.73\mu m$, $\sigma = 1.36\mu m$ (Polysciences Inc. 64155) in phosphate-buffered saline at a concentration of 5×10^5 particles/mL. In addition, Bovine Serum Albumin is mixed into the particle solution at a final concentration of 1% to coat particles and prevent against clogging and multiparticle aggregates from forming. We flowed this mixture of microspheres through three device designs (Fig. 6 row one): MB length 7, MB length 11, and MB length 13. A flow controller (Elveflow OB1 MK3) was used to apply 70 mbar of pressure through the channel, resulting in a flow rate close to 2$\mu l/min$. We have modeled using Comsol Multiphysics 5.0 the fluid flow in the three MB encoded channels that we measured to ensure that inertial flow focusing does not occur. As shown in

Supplementary Section V the flow remains laminar throughout the device and no vortices are formed. Finally, we apply Ohm's law to our current measurements to obtain the impedance response and decimate our signal by a factor of 15 to get samples at an equivalent rate of 3.33 kHz.

VI. Results

A. Simulations and Estimator Analysis

In this section we analyze our processing system in terms of the bias and variance of the estimated pulse heights and transit-times of particles. In addition, we study how reliably our system can detect particles in a coincidence event. The practical issues governing these parameter estimators' performance are the various system model errors present in the measured signal as well as noise. These result in bias in the pulse-height estimates, variance in transit-time estimates, and decreased dynamic range of reliable detections as compared to an ideal system. To evaluate the performance of our system for the different non-idealities, we created a tool for simulating the system response of our NPS experimental setup.

Our simulation tool focuses on mimicking both the deterministic and stochastic components of our system. The tool is parametric with deterministic channel specific parameters (z_{geo}, a vector containing the node pore ordering and the length of each node or pore in the channel encoding) and experimental specific parameters (pulse height, α, transit time through the channel, τ). The resulting ideal system model simulation, $x(\alpha, \tau, z_{geo})$, is sampled at 50kHz. In addition, smooth transition response from nodes to pores (node-pore) and visa versa is accounted for by convolving $x(\alpha, \tau, z_{geo})$ with a normalized Hanning window, k, with a length that is a percentage of the total length of the system response.

Stochastic system model components for additive noise and random particle-channel interactions are included. Additive white Gaussian noise (AWGN) with zero mean and unit variance is scaled to experimentally observed levels, σ_{exp}, and added to the simulation. Particle-channel interactions manifest by manipulating the channel geometry, now represented z_{stoch}, which is a random vector according to a uniform distribution with mean z_{geo} and spread ± a percentage of the total length of the system response. These factors are summarized below in Equation 9.

$$y_{t,\,sim} = k * x\left(t, \alpha, \tau, z_{stoch}\right) + \sigma_{exp} n_t \quad (9)$$

B. Pulse-Height Analysis

To isolate and analyze the effect of MB code non-idealities, which we attempt to mitigate via robust regression, we performed a simulation experiment mimicking our experimental system. We simulated instances of non-overlapping particles going through MB length 7, 11, 13 encoded channels of the same length that yield a transit time of 150 ms (the average observed transit time for our experiments outlined in Section V). The random particle-channel interactions are accounted by uniformly varying the channel geometry, z_{geo} by 1% the total response length and the node-pore transition kernel has length 0.5% the total response length. The simulated pulses were evaluated at 50KHz sampling rate and down-sampled to a rate of 3.333kHz. A range of relevant particle sizes were simulated by varying the pulse height of signatures simulated. In order to match our experimental data, the AWGN is scaled to have a standard deviation matching that of the experiments, $\sigma_{exp} = 1.24 \times 10^{-4}$ such that the range of pulse heights correspond to a range of SNRs from 0-30 dB. This is the observed range of SNR for the particle sizes in our experiments outlined in Section V. Baseline drifts were not simulated here, as their effect is isolated in the regression performed in Equation 6 and Equation 8. For each particle size, a 1000 signatures were generated, from which the pulse heights were estimated with both the least-squares and the robust regression techniques. The sample bias and variance of the estimates were then computed.

Figure 5 highlights the imperfections' effects on the bias and variance estimator metrics of the least-square pulse-height estimate side-by-side with our proposed robust regression pulse-height estimate. The blue curves in Figure 5 show the bias and variance for ideal responses with varying noise and without stochastic and node-pore transition effects. In that case, a least-square regression would be suitable for pulse-height estimation. However, in the presence of the system model imperfections, the least-squares fit would induce significant additional bias and variance in pulse height estimates, as visualized by the red curves in Figure 5. In contrast, our method of robust regression (yellow curves in Figure 5) provides a reduction in estimation bias and variance over the least-square pulse height estimates on simulated signals with imperfections over a relevant range of SNR, which correspond to particle size. Another important observation that is seen in Figure 5 is that the robust regression plays a more important role in the longer codes, MB length 11 and 13. These more complex codes are more susceptible system model error as they exhibit many more node-pore transitions.

C. Transit-Time Analysis

To analyze the effect of MB code non-idealities on our ability to estimate the transit time through the device, we perform a simulation to empirically measure this estimator's bias and variance. Again, we simulated instances of non-overlapping particles going through MB length 7, 11, 13 encoded channels, but now rather with the transit time of 150.0 ms, 25% faster (112.5 ms), and 25% slower (187.5 ms) (the observed range of transit time for our experiments outline in Section V-B). The random particle-channel interactions and node-pore transitions are accounted for with the same parameters as in Section VI-B. The simulated pulses were evaluated at 50KHz sampling rate and down-sampled to a rate of 3.333kHz. The pulse height simulated was set be $4m\Omega$, corresponding to $15\mu m$ particles and held constant, as this parameter minimally effects the estimate of transit time. Again, baseline drifts were not simulated here because their effects are isolated in the regression performed in Equation 6 and equation 8. The simulated signals' transit times (a 1000 signatures per transit time) were then estimated by applying a matched filter bank with 500 filters evenly spaced from 30ms to 270ms and selecting the transit time corresponding to the matched filter with the maximum response.

Table 1 highlights the variability of the transit-time estimator through the sample mean and sample variance (See supplementary for histograms visualizing this analysis). Much as in the case for amplitude estimation, the longer codes demonstrated slightly more sensitivity to the stochastic variations, highlighted by the increased variances. Additionally, we observe that slower particles have a greater absolute error in transit time than faster particles, but have the same relative error. This estimator analysis helps us choose the correct number of filters to discretize our transit time parameter space. The variability due to non-idealities determines the upper bound on our estimator's resolution, thus telling us the fewest number of filters we need to accurately estimate transit time. It also suggests that the transit time resolution of the filter bank can be coarser for slow transit time and finer for the faster transit times.

D. Dynamic Range Analysis in Coincidence events

Any model mismatch in the SIC process would yield a residual error that could inhibit the detection of signals from smaller particles. The level of this residual, which could be modeled as stochastic interference in the correlations with the matched filter-bank would effectively determine the lower bound on the dynamic range of reliable detections in coincidence events. For example, the residuals from a mismatched estimate of a $15\mu m$ particle could potentially mask-out the peak correlation of particles smaller than a colloquial $5\mu m$ particle – thus limiting the dynamic range in a coincidence event with the $15\mu m$ particle to detecting particles larger than $5\mu m$. Alternatively, the same residual energy could correlate with the matched filter bank and cause a false alarm detection of a $5\mu m$.

To analyze the effect of MB code non-idealities on our ability to detect particles in coincidence settings, we manually selected $10\mu m$ and $15\mu m$ non-coincident detections from each experimental setup: MB length 7 (32 and 14 counts respectively), 11 (30 and 37 counts respectively), and 13 (27 and 29 counts respectively) in post processing. We perform the same processing as outlined in algorithmic methods on each selected detection with a stopping criteria of 6 SIC iterations. From the processing we expect exactly a single true detection to be present. All successive detections that are found are false alarms and can be used to estimate a distribution of false alarms.

Table 2 reports the sample mean and sample standard deviation statistics of false-alarm detections from an MB length 7, 11, and 13 experiments for selected $10\mu m$ and $15\mu m$ particles (See supplementary for histograms visualizing this analysis).Thresholds are derived from these statistics in Section VI-E to prune false alarm detections. These thresholds represent possible lower bounds on the dynamic range of particle sizes that we can detect in coincidence settings with an acceptable number of false alarms detections.

E. Experimental Microsphere Results

Experiments were conducted as outlined in Section V, raw data was processed with methods outlined in Section III, and results are presented in Figure 6d-l. We separated the detections to those with and without coincidence events. In the non-coincidence detections, visualized in Figure 6d-f, distinctive clusters of three differently sized particles are detected. In the coincident setting, visualized in Figure 6g-i, the lower range of particle sizes is flooded with spurious false alarms and only two of the larger distinctive clusters are present. Motivated by the unreliable detection of smaller particles, detection pruning based on pulse-height amplitude is performed on coincidence event detections, according to analysis in Section VI-D and with results displayed in Figure 6j-l. Coincidence detections in the presence of 10*μm* and 15*μm* particles are pruned if their amplitude is less than thresholds derived from analysis in Section VI-D. From Figure 6, we report 5*μm*, 10*μm*, and 15*μm* diameter non-coincidence and coincidence event detected particle counts for MB length 13 (27, 161, 86), MB length 11 (78, 228, 116), and MB length 7 (100, 158, 34). Further highlighted in Figure 6 is the wider spread of transit time for 5*μm* and 10*μm* particle distributions. This could be due to the parabolic flow profile [48] across the cross section of the channel. This would cause the flow-rate to vary away from the central axis of the channel, so while the larger particles remain in the center, smaller particles could move off-axis and experience slower flow-rates.

As discussed earlier, the gain in SNR is due to the properties of matched filtering, and is specifically helpful when detecting 5*μm* diameter particles. These particles have low SNR (~ 1 dB) in the measured signal and show improved SNR (~ 23 dB) after matched filtering. Average SNR for the detected 5*μm*, 10*μm*, and 15*μm* particles (Fig. 6) are reported in Table 3 in the measured impedance domain and in the matched-filter domain (counts for these averages were reported above). Further, Figure 7 visualizes this SNR gain with experimental impedance signatures in the left column and matched-filtered responses of the same experimental data in the right column. In addition, the left column of Figure 7 highlights the wide dynamic range of pulse heights we observe for particles of 5*μm* (top row), 10*μm* (middle row), 15*μm* (bottom row) diameters transiting our channels.

The gain in temporal resolution due to matched filtering is discussed theoretically in Section II and is observed experimentally and highlighted in Figure 8. For a constant length channel, MB length 7, 11, and 13 have increasingly finer temporal resolution inversely proportional to their code's BW. Specifically, the FWHM of each correlation peak in Figure 8 decreases as their respective code's BW increases.

VII. Discussion

Our MB codes can be characterized by their temporal resolution and number of symbols. The temporal resolution of a code is determined by the symbol transit time and is controlled by the flow speed and channel's dimensions. These specifications are often application specific parameters, thus special consideration is required when deciding which code to use in a specific instance.

For a device of fixed length, the MB 13 encoding will have the finest temporal resolution. The minimum symbol length is limited by the diameter of the particles that are being sized. The symbol length must be several times longer than the particles' diameter, such that modulation of the signal when transiting from node to pore still occurs. Failure to do so will result in symbol pulses that are not sharp and pronounced, leading to induced system-modeling error. When the minimum symbol length cannot be met and shorter device are desired, then shorter MB codes (i.e. MB length 7 and MB length 11) should be used to encode the channel.

As channel length further increases and the proposed set of MB codes are dilated to fit the longer channels, desired temporal resolution will decrease and an increased number of coincidence events could be observed. Applications requiring significantly longer channels will require a new set of more advanced codes to achieve the same temporal resolution, as the longest known Barker sequence has length 13. These longer codes will have less favorable quasi-orthogonality properties than our proposed set of codes, but could still be effective in providing both a gain in SNR and temporal resolution. Possible candidates for longer sequences with similar but sub-optimal properties [51] include maximum length sequences [52], Gold sequences [53], and sequences that are comprised of non-binary symbols [51].

Experimental data has validated our methods and has driven important modifications and analysis to our algorithmic methods. We observed that decreased bias due to the robust regression (in agreement with our simulation) is the most important factor in mitigating the effect of system modeling error. Without this component, significant energy is left in the residual signal that well correlates with the system model resulting in false alarms. We believe, based on our analysis in Section VI-D, that false alarms determine the dynamic range's lower limit of detectable particle size in coincidence events and are the limiting factor of channel-encoding methods for individual particle coincidence correction.

Our analysis, based on simulations with experimentally relevant parameters, suggests several trends that could influence code selection. While more complex codes (i.e. MB length 11 and 13) provide a finer temporal resolution and a less pronounced sidelobes than MB length 7 encoding, they are more susceptible to channel and flow non-idealities due to the increased number of node-pore transitions. These non-idealities manifest themselves as a combination of errors: increased pulse height estimator bias, increased transit time estimator variance, and an increased number of false alarm detections.

We have experimentally observed several other areas of deviation from the ideal system model: large particles' node responses do not completely return to baseline, pulse heights can vary from pore to pore within a single particle response, and the node-pore transitions are not instantaneous, but smooth. It is possible that these observed non-idealities are the result of off-axis affects [48] and could be modeled with additional dimensions in the filter bank. However, affects that are not properly modeled or handled with the calibration will continue to effect device performance and motivates being robust to them (ie. robust regression fitting).

When choosing device dimensions and flow specifications for specific application it is important to consider the boundary conditions of the device. The largest expected particle size must be considered so that the minimum pore width and height does not cause clogging of the channel and so that the node width allows the impedance signal to return to baseline. Based on the width of the nodes, the length of the pores should be set so that a particle's transit time in nodes and pores are near equal to enable the maximum benefits of matched filtering. However, exact matching of node and pore transit times is not required as model calibration will account of global variations. For high throughput applications, it is important to consider the effect of high flow rate which would cause inertial flow focusing as described in Yang et al.[6] and Amini et al. [54] and micro-scale vortices in certain dimension nodes as described in Sollier et al.[55].

VIII. Conclusions

We have demonstrated that by encoding a microfluidic channel with a MB code arrangement of nodes and pores, we have the ability to increase the sensitivity of the device to smaller particles and to provide individual particle coincidence correction. Both are enabled by the joint design of the channel and the sparse deconvolution algorithm. We identify several sources of modeling error and mitigate most effects via a data-driven system model calibration step and robust model regression. We analyze the performance of our method to estimate particle size and transit time as well as the effective dynamic range of particle sizes we can reliably detect in coincidence settings. Finally, we experimentally validate several channel designs that fit in our framework by screening a heterogeneous sample of several size particles through them.

Supplementary Material

Refer to Web version on PubMed Central for supplementary material.

Acknowledgments

This work was funded in part by NIH R21EB01981-01A1 (L. L. S. and M. L.) and NSF ECCS 1509921 (L. L. S. and M. L.). M. K. is supported through a NSF Graduate Research Fellowship (DGE 1106400). Special thanks to Junghyun Kim for performing Comsol flow simulations of the three device configurations.

References

1. Coulter WH. Means for Counting Particles Suspended in a Fluid. Jul.1953 :1–9.
2. Graham MD. The Coulter principle: foundation of an industry. Journal of the Association for Laboratory Automation. Dec; 2003 8(6):72–81.
3. Coulter WH. High Speed Automatic Blood Cell Counter and Cell Size Analyzer. Oct.1956 :1–11.
4. Brecher G, Scheiderman M, Williams G. Evaluation of Electronic Red Blood Cell Counter. Dec. 1956 :1–11.
5. Mattern C, Brackett F, Olson B. Determination of Number and Size of Particles by Electrical Gating: Blood Cells. Jun.1956 :1–15.
6. Yang, D., Leong, S., Lei, A., Sohn, LL. High-throughput microfluidic device for rare cell isolation. In: van den Driesche, S., editor. SPIE Microtechnologies. SPIE; Jun, 2015
7. Chapman, MR., Sohn, LL. Methods in Cell Biology. 2nd, ser. Vol. 102. Elsevier Inc.; May, 2011 Label-Free Resistive-Pulse Cytometry.
8. Yang L, Bashir R. Electrical/electrochemical impedance for rapid detection of foodborne pathogenic bacteria. Biotechnology Advances. Mar; 2008 26(2):135–150. [PubMed: 18155870]
9. Sarioglu AF, Aceto N, Kojic N, Donaldson MC, Zeinali M, Hamza B, Engstrom A, Zhu H, Sundaresan TK, Miyamoto DT, Luo X, Bardia A, Wittner BS, Ramaswamy S, Shioda T, Ting DT, Stott SL, Kapur R, Maheswaran S, Haber DA, Toner M. A microfluidic device for label-free, physical capture of circulating tumor cell clusters. Nature Methods. May; 2015 12(7):685–691. [PubMed: 25984697]
10. Au SH, Storey BD, Moore JC, Tang Q, Chen YL, Javaid S, Sarioglu AF, Sullivan R, Madden MW, Keefe RO, Haber DA, Maheswaran S, Langenau DM, Stott SL, Toner M. Clusters of circulating tumor cells traverse capillary-sized vessels. Proceedings of the National Academy of Sciences. May; 2016 113(18):4947–4952.

11. Holmes D, Pettigrew D, Reccius CH, Gwyer JD, van Berkel C, Holloway J, Davies DE, Morgan H. Leukocyte analysis and differentiation using high speed microfluidic single cell impedance cytometry. Lab on a Chip. 2009; 9(20):2881–10. [PubMed: 19789739]
12. Kasianowicz J, Brandin E, Branton D, Deamer DW. Characterization of individual polynucleotide molecules using a membrane channel. Proc Natl Acad Sci. Nov.1996 93:13 770–13 773. [PubMed: 8552589]
13. Kozak D, Anderson W, Vogel R, Trau M. Advances in resistive pulse sensors: Devices bridging the void between molecular and microscopic detection. Nano Today. Oct; 2011 6(5):531–545. [PubMed: 22034585]
14. Peng R, Li D. Detection and sizing of nanoparticles and DNA on PDMS nanofluidic chips based on differential resistive pulse sensing. Nanoscale. 2017; 9(18):5964–5974. [PubMed: 28440838]
15. Lan F, Demaree B, Ahmed N, Abate AR. Single-Cell Genome Sequencing at Ultra-High-Throughput with Microfluidic Droplet Barcoding. Nature Publishing Group. May.2017 :1–10.
16. Venkatesan BM, Bashir R. Nanopore sensors for nucleic acid analysis. Nature Publishing Group. Sep; 2011 6(10):615–624.
17. Reccius CH, Stavis SM, Mannion JT, Walker LP, Craighead HG. Conformation, Length, and Speed Measurements of Electrodynamically Stretched DNA in Nanochannels. Biophysical Journal. Jul; 2008 95(1):273–286. [PubMed: 18339746]
18. Phipps LW, Newbould FHS. Determination of leucocyte concentrations in cow's milk with a Coulter counter. doi org. 1966:1–14.
19. Mullin JW, Ang HM. Crystal Size Measurement: Comparison of the Techniques of Sieving and Coulter Counter. Powder Techology. Feb.1974 :153–156.
20. Wales M, Wilson JN. Theory of Coincidence in Coulter Particle Counters. Review of Scientific Instruments. Oct; 1961 32(10):1132–1136.
21. Wales M, Wilson JN. Coincidence in Coulter Counters. Review of Scientific Instruments. May; 1962 33(5):575–576.
22. Samyn JC, McGee JP. Count Loss with the Coulter Counter. Journal of Pharmaceutical Science. Nov; 1965 54(12):1794–1799.
23. Princen LH, Kwolek WF. Coincidence Corrections for Particle Size Determinations with the Coulter Counter. Review of Scientific Instruments. May; 1965 36(5):646–653.
24. Lewis SM, England JM, Kubota F. Coincidence Correction in Red Blood Cell Counting. Physics in Medicine and Biology. Mar; 1989 35(8):1159–1162.
25. Kersting K. Specific Problems Using Electronic Particle Counters. Hydrobiological Bulletin. 1985:5–12.
26. Coulter Principle Short Course. Tech Rep. 2014
27. DxH 500 Hematology Series. Tech Rep. 2015
28. Beckman Coulter Z Series. 1997
29. Zhe J, Jagtiani AV, Dutta P, Hu J, Carletta J. A Micromachined High Throughput Coulter Counter for Bioparticle Detection and Counting. Journal of Micromechanics and Microengineering. Jun; 2006 16(8):1530–1539.
30. Jagtiani AV, Carletta J, Zhe J. A Microfluidic Multichannel Resistive Pulse Sensor Using Frequency Division Multiplexing for High Throughput Counting of Micro Particles. Journal of Micromechanics and Microengineering. Mar; 2011 21(4):045 036–11.
31. Liu R, Wang N, Kamili F, Sarioglu AF. Microfluidic CODES: a scalable multiplexed electronic sensor for orthogonal detection of particles in microfluidic channels. Lab on a Chip. Apr; 2016 16(8):1350–1357. [PubMed: 27021807]
32. Liu R, Waheed W, Wang N, Civelekoglu O, Boya M, Chu CH, Sarioglu AF. Design and modeling of electrode networks for code-division multiplexed resistive pulse sensing in microfluidic devices. Lab on a Chip. Jul.2017 17:2650–2666. [PubMed: 28695944]
33. Javanmard M, Davis RW. Coded Corrugated Microfluidic Sidewalls for Code Division Multiplexing. IEEE Sensors Journal. Mar; 2013 13(5):1399–1400.
34. Polling D, Deane SC, Burcher MR, Glasse C, Reccius CH. Coded Electrodes for Low Signal-Noise Ratio Single Cell Detection in Flow-Through Impedance Spectroscopy. Jul.2010 :1–3.

35. Xie P, Cao X, Lin Z, Talukder N, Emaminejad S, Javanmard M. Processing gain and noise in multi-electrode impedance cytometers: Comprehensive electrical design methodology and characterization. Sensors & Actuators: B Chemical. Mar.2017 241:672–680.

36. Kellman M, Rivest FR, Pechacek AP, Lustig M, Sohn LL. Barker-Coded Node-Pore Resistive Pulse Sensing with Built-in Coincidence Correction. Dec.2017 :1–5.

37. Goldsmith, A. Wireless Communications. Cambridge University Press; 2005.

38. Balakrishnan KR, Whang JC, Hwang R, Hack JH, Godley LA, Sohn LL. Node-Pore Sensing Enables Label-Free Surface-Marker Profiling of Single Cells. Analytical Chemistry. Mar; 2015 87(5):2988–2995. [PubMed: 25625182]

39. Balakrishnan KR, Anwar G, Chapman MR, Nguyen T, Kesavaraju A, Sohn LL. Node-pore sensing: a robust, high-dynamic range method for detecting biological species. Lab on a Chip. 2013; 13(7):1302–6. [PubMed: 23386180]

40. Barker RH. Group synchronizing of binary digital systems. Communication Theory. :273–287.

41. Deblois RW, Bean CP, Wesley RKA. Electrokinetic measurements with submicron particles and pores by the resistive pulse technique. Journal of Colloid and Interface Science. Sep; 1977 61(2): 323–335.

42. Ohrtman, FD., Roeder, K. Wi-Fi Handbook: Building 802.11b Wireless Networks. 1st. New York: McGraw-Hill Inc; 2003.

43. Richards MA. Fundamentals of radar signal processing Tata McGraw-Hill Education. 2005

44. Levanon N. Noncoherent Pulse Compression. IEEE Transactions on Aerospace and Electronic Systems. Apr.2006 :756–765.

45. Stallings, W. Data and Computer Communications. 8th. Pearson Education; 2007.

46. Tropp JA, Gilbert AC. Signal Recovery From Random Measurements Via Orthogonal Matching Pursuit. IEEE Transactions on Information Theory. Dec; 2007 53(12):4655–4666.

47. Blake S. OS-CFAR Theory for Multiple Targets and Nonuniform Clutter. IEEE Transactions on Aerospace and Electronic Systems. Nov; 1987 24(6):785–790.

48. Saleh OA, Sohn LL. Correcting off-axis effects in an on-chip resistive-pulse analyzer. Review of Scientific Instruments. Dec; 2002 73(12):4396–4398.

49. Andersen, R. Modern Methods for Robust Regression. Sage; 2008.

50. Daubechies I, Devore R, Fornasier M, Gunturk CS. Iteratively Reweighted Least Squares Minimization for Sparse Recovery. Pure and Applied Mathematics. Oct.2009 :1–38.

51. Jedwab J. What can be used instead of a Barker sequence? Contemporary Mathematics. Feb.2008 : 1–26.

52. Golomb, SW., Gong, G. For Wireless Communication, Cryptography, and Radar. Cambridge University Press; 2005. Signal Design for Good Correlation, ser.

53. Gold R. Optimal Binary Sequences of Spread Spectrum Multiplexing. IEEE Transactions on Information Theory. 1967; 13:619–621.

54. Amini H, Lee W, Di Carlo D. Inertial microfluidic physics. Lab Chip. 2014; 14(15):2739–23. [PubMed: 24914632]

55. Sollier E, Go DE, Che J, Gossett DR, O'Byrne S, Weaver WM, Kummer N, Rettig M, Goldman J, Nickols N, McCloskey S, Kulkarni RP, Di Carlo D. Size-selective collection of circulating tumor cells using Vortex technology. Lab Chip. 2014; 14(1):63–77. [PubMed: 24061411]

Biographies

Michael R. Kellman received his B.S. in Electrical and Computer Engineering from Carnegie Mellon University in 2015. Since 2015, he has been working towards his M.S. and Ph.D. in the department of Electrical Engineering and Computer Science at the University of California, Berkeley, where his research is focused on applying signal processing and optimization methods to novel applications.

Francois R. Rivest received his B.S. and M.S. in Life Sciences and Bioengineering, from the Swiss Federal Institute of Technology in Lausanne (EPFL) in 2012 and 2015, respectively. Since, he has been working toward a Ph.D. in Biotechnologies and Bioengineering with Prof. Lydia Sohn, at UC Berkeley, and with Prof. Lutolf, at EPFL, where he has been working on single cell screening platforms and their applications for stem cell and cancer research.

Alina Pechacek received her B.S. in Engineering from Smith College in 2013 and M.S. from the department of Electrical Engineering and Computer Science at the University of California, Berkeley in 2016. Currently, she is working at MITRE as a signal processing engineer.

Lydia L. Sohn received her A.M. and Ph.D. in Physics from Harvard University in 1990 and 1992, respectively. Since 2003, she has been a professor of Mechanical Engineering at the University of California, Berkeley, where her research focuses developing microfluidic applications for biomedical research and clinical diagnostics. She currently holds 3 US Patents and is a Fellow of the American Institute for Medical and Biological Engineering.

Michael (Miki) Lustig is an Associate Professor in EECS. He joined the faculty of the EECS Department at UC Berkeley in Spring 2010. He received his B.Sc. in Electrical Engineering from the Technion, Israel Institute of Technology in 2002. He received his Msc and Ph.D. in Electrical Engineering from Stanford University in 2004 and 2008, respectively. His research focuses on computational imaging methods in medical imaging, particularly Magnetic Resonance Imaging (MRI).

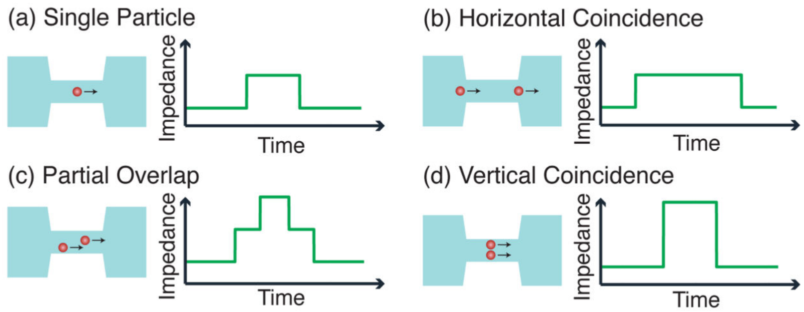

Fig. 1.

Illustration of Coincidence Events: (a) a single particle transiting the channel, (b) horizontal coincidence of two particles, (c) partial coincidence of two particles, (d) vertical coincidence of two particles.

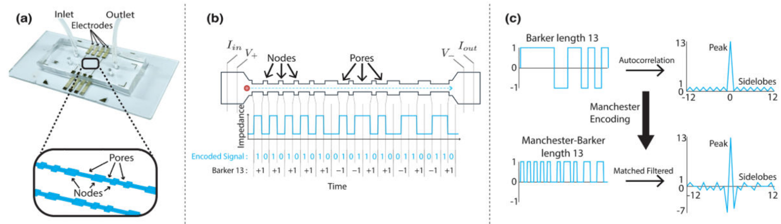

Fig. 2.

Device and Code Design: (a) A photograph of a pair of polydimethylsiloxane (PDMS) channels encoded with wider (nodes) and narrower (pores) regions bonded to a glass substrate with a pair of electrodes. The zoomed in region of photograph highlights a portion of the computer aided design schematic of the two channels' interleaved nodes and pores. (b) The top view of a channel as a single particle transits and the expected impedance signature from the Manchester-Barker length 13 encoding sequence. Vertical dashed lines highlight the correspondence between segments of the channel and the binary code. (c) Quasi-orthogonality (pulse compression) properties of the transitional Barker length 13 sequence and the Manchester-Barker length 13 sequence we utilize to encode our channels.

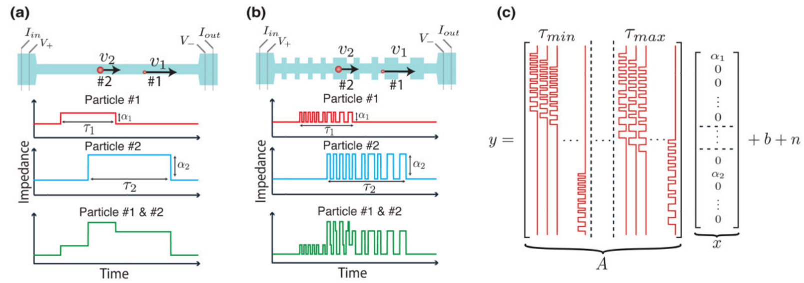

Fig. 3.

Coincidence Event and Forward Model Construction: (a) a traditional Coulter-counter channel and (b) a Coulter-counter MB length 13 encoded channel and their resultant impedance signals during coincidence event. In this coincidence event, a smaller faster particle #1 travels at a speed of v_1 and generates a pulse with height α_1 and duration τ_1 and a larger slower particle #2 travels at a speed of v_2 and generates a pulse with height α_2 and duration τ_2. (c) An illustration of the decomposition of the signal resulting from the coincidence event in (a) into Equation 3: a forward model, A, a sparse vector, x, a baseline, b, and a noise term, n. The forward model is a dictionary of channel response signals parametrized by arrival and transit-time. x is a sparse vector representing individual particle's amplitudes at indices representing the arrival and transit time of these particles.

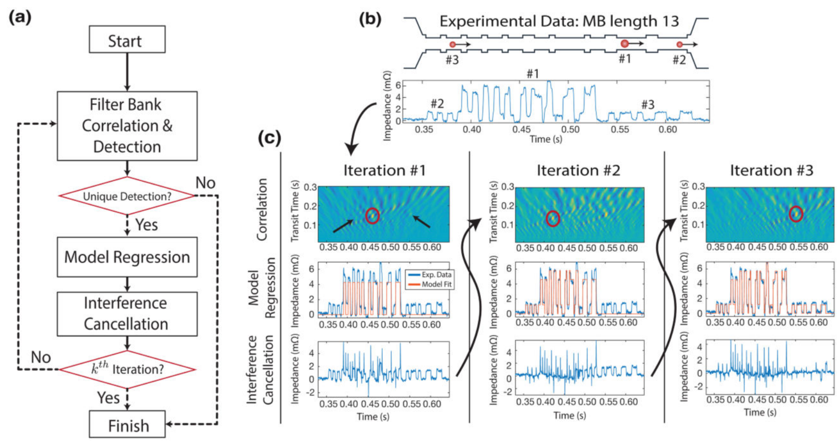

Fig. 4.

Successive Interference Cancellation Method: (a) Flow chart of our iterative SIC algorithm that solves the sparse deconvolution problem posed in Equation 4. (b) Illustration of coincidence event of a larger particle (#1) with two smaller particles (#2,#3) and a piece of experimental data (outlined in Section V) from a MB length 13 encoded channel. (c) Step-by-step figures of three iterations of our algorithm applied to experimental data in part b, (top row) correlation with MB length 13 code's matched filter bank and circled (red) detection of peak at arrival and transit time of the current iteration's detected particle. Small black arrows indicate undetectable particles in first iteration. (middle row) overlaid fitted detected model components to experimental data, (bottom row) cancelled interference from iteration's current model fit. The cancelled interference signal from previous iteration is used as input to the next iteration.

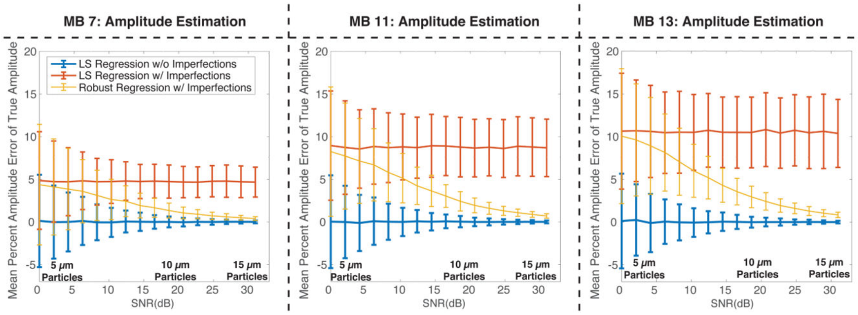

Fig. 5.

Pulse-Height Estimator Analysis: Effects of ideal (blue curves) versus simulated (red curves) system-model error on least-squares (LS) pulse-height estimation compared to the effects of simulated system-model error on the robust regression (yellow curves) pulse-height estimation. Estimator bias in percent error from the simulated is plotted as a function of the particle's SNR (dB) for MB length 7, 11, 13 encoded channels. This is the observed range of SNR for the particles in our experiments outline in Section V-B. Error bars represent one standard deviation of variability in the error of our estimate.

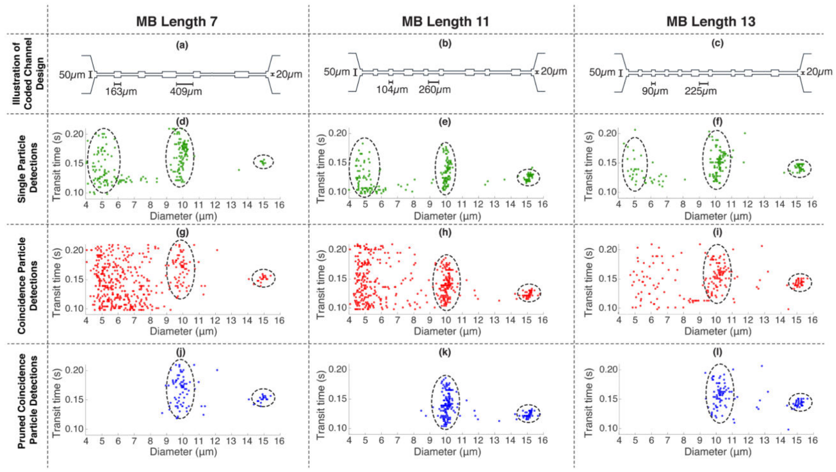

Fig. 6.

Experimental Microsphere Results: (a-c) coded channel designs for MB length 7, 11, 13, respectively, (d-f) single particle detections for MB length 7, 11, 13, respectively, (g-i) coincidence particle detections for MB length 7, 11, 13, respectively, (j-l) pruned coincidence particle detections for MB length 7, 11, 13, respectively.

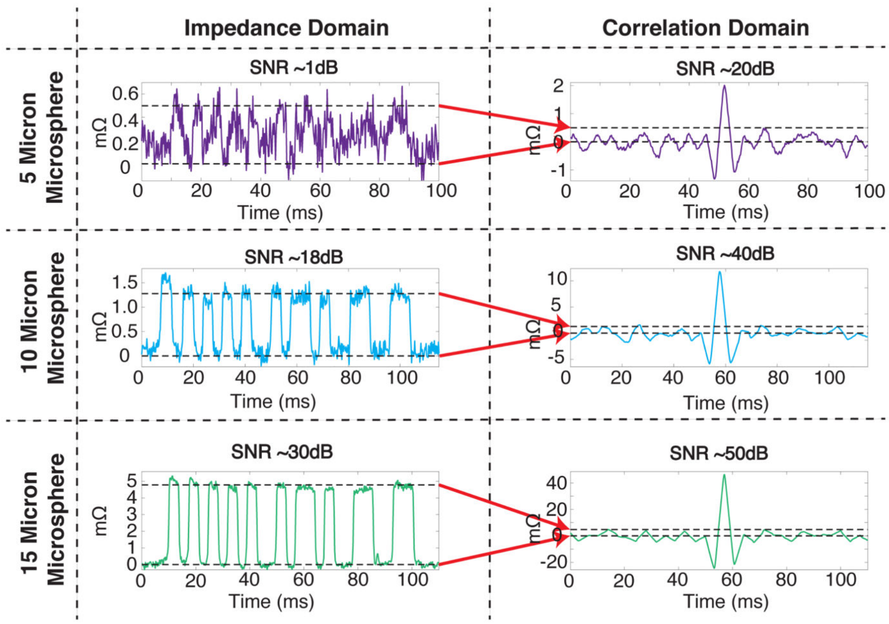

Fig. 7.

Experimental Matched Filtering Results: Example impedance responses from 5μm, 10μm, 15μm particles transiting a MB length 13 encoded channel (from experiments outlined in Section V) and their matched-filter response. Red arrows emphasize the scale at which match filtering is able to boost SNR.

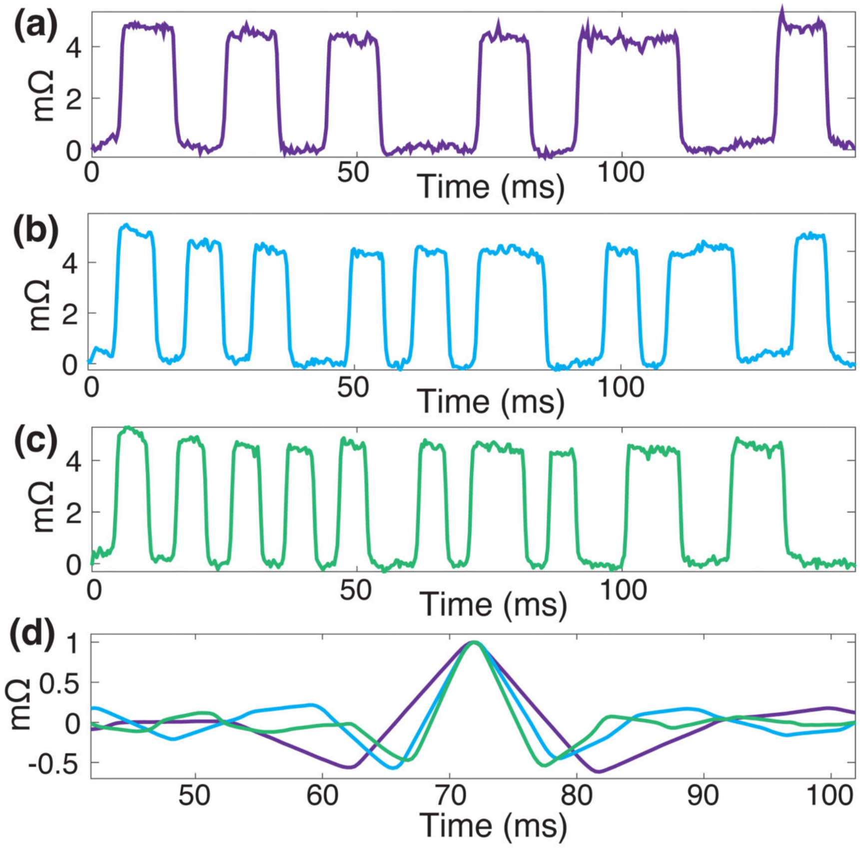

Fig. 8.

Experimental Temporal Resolution Results: Experimental channel responses (from experiments outlined in Section V) for 15*μm* particles for MB length 7 (a), 11 (b), 13 (c) codes and the overlay of their matched filter responses (d). Curve colors in panel d correspond to the different code's colors in panels a through c.

Table 1

Transit-Time Error Statistics: Sample mean and sample variance statistics of transit-time error as a percent of true transit time for a range of transit times: 187.5 ms (left column), 150.0 ms (middle column), and 112.5 ms (right column) for each channel encoding: MB-length 7 (top row), 11 (middle row), 13 (bottom row). This is the observed range of transit times in our experiments as outlined in Section V-B.

(Mean %, Variance %)			
Transit Time (*ms*)	**187.5**	**150.0**	**112.5**
MB length 7	(-0.09, 1.18)	(-0.12, 1.07)	(-0.22, 1.19)
MB length 11	(0.01, 1.75)	(-0.09, 1.61)	(-0.04, 1.70)
MB length 13	(0.12, 2.09)	(0.08, 2.03)	(-0.03, 2.17)

Table 2

False Alarm Distribution Statistics: Sample mean and sample standard deviation of false alarm distributions in presence of manually selected experimental 10*μm*, and 15*μm* true detections for MB length 7, 11, and 13 encoded channels.

(Mean (*μm*), Standard Deviation (*μm*))		
	10 μm particles	***15 μm particles***
MB length 7	(4.68, 0.89)	(6.67, 1.09)
MB length 11	(5.49, 0.63)	(7.26, 1.04)
MB length 13	(4.71, 0.97)	(6.89, 1.17)

Author Manuscript

Author Manuscript

Author Manuscript

Table 3

Signal to Noise Ratio Analysis: Average experimental impedance-domain SNR for 5μm, 10μm, 15μm diameter particles for each encoding configuration, experimental matched-filter domain SNR for 5μm, 10μm, 15μm diameter particles for each encoding configuration. Particles from non-coincident and coincident events are included in these averages and counts are reported in Section VI-E.

	Size (μm)	MB 7	MB 11	MB 13
Impedance SNR (dB)	5	1.77	18.89	30.52
	10	1.61	19.33	30.94
	15	2.18	18.47	30.33
Matched Filter SNR (dB)	5	22.93	39.98	51.55
	10	24.10	39.69	51.08
	15	23.08	39.57	51.23